Nonisothermal Parison Inflation in Blow Molding

Nonisothermal inflation of a viscous annular parison and its cooling and solidification before and upon wall contact are analyzed by solving the unsteady momentum and energy conservation equations. The algorithm simultaneously determines the flow field and temperature distribution within the parison together with the moving surfaces at every time step. Results of the present study indicate that the inflation rate is increased as a result of higher temperature within the parison. However, the instantaneous shape of the parison and the final thickness variation upon mold contact remain virtually unchanged. Due to the temperature dependence of physical properties, the critical factor during inflation is initial temperature distribution within the parison. Inflation resulting in full attachment to a confining mold wall takes only a small fraction of the time required to cool the material to the ambient gas temperature. The transient calculations illustrate how computer simulations may be used to improve design of blow molding operations, and they are in good agreement with available experiments.

Andrew J. Poslinski
John A. Tsamopoulos
Department of Chemical Engineering
State University of New York
Buffalo, NY 14260

Introduction

Blow molding operations involve the unsteady and nonisothermal inflation of a fluid meniscus. The meniscus, or parison, of molten material is extruded from an annular die or is injection-molded around a solid core rod and may have an annular or axisymmetric shape. Two mold halves close on the parison, clamping it around its edges and separating it from the rest of the material. The stages of injection blow molding are shown in Figure 1. The parison is forced by external air pressure to deform and take the shape of the confining mold cavity. Simultaneously, it is cooled and becomes solidified primarily due to heat loss to the cooled walls. The finished product is ejected to produce a thin-wall container or structural part. Due to the low thermal conductivity of polymeric liquids typically used in the process, the cooling stage in blow molding accounts for a large portion of the production cycle. In addition, the physical properties of the molten material critically depend on the temperature distribution within the meniscus. Therefore, solidification during and after inflation not only affects and sometimes determines mold design and production cycle time, but also results in anisotropic physical and mechanical properties of the final product. Furthermore, the mechanical strength of an inflated part is largely dependent on its thickness distribution, and since a product with a very thick wall is uneconomical, the most desirable shape is never far away from that of uniform thickness. Unlike injection molding, in blow molding the thickness of the final product cannot be controlled by the mold shape alone. Instead, it may be necessary to employ accurately programmed extrusion of material from dies of different geometries, resulting in parisons of increased thickness at prespecified locations. Thus, excessive thinning of material that eventually fills edges or corners of the mold can be compensated. All these factors must be taken into account in an attempt to optimize the process. In practice, a trial-and-error procedure is used whereby at each step either the shape of the meniscus prior to inflation is varied, the process conditions are adjusted, or a new set of mold configurations is produced until a satisfactory product is obtained. This slow and very expensive approach could be significantly improved by a reliable, computer-aided design method based on numerical simulation of the nonisothermal inflation stage.

Previous theoretical attempts have relied on simplified one-dimensional models for meniscus cooling and inflation based only on mass conservation principles (C. D. Denson, 1973; Ryan and Dutta, 1982; Edwards et al., 1979). Clearly, such models

Correspondence concerning this paper should be addressed to J. A. Tsamopoulos.
The present address of A. J. Poslinski is GE Corporate Research & Development, P.O. Box 8, Schenectady, NY 12301.

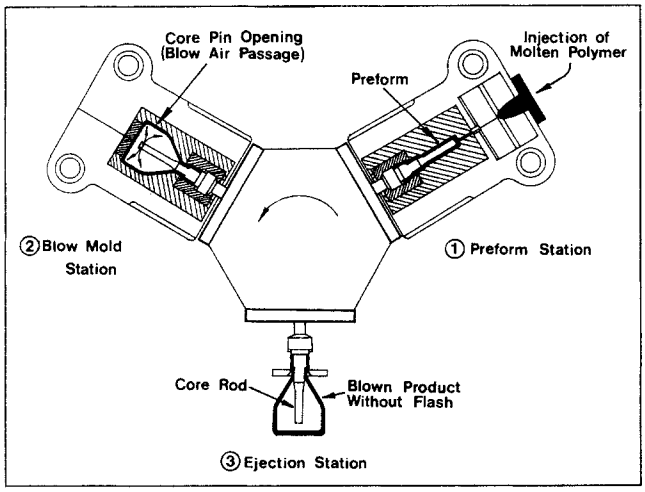

Figure 1. Extrusion blow molding process.

are unable to predict operating times and realistic shapes of different materials, or match other experimental observations in complicated forming operations. Along the same lines, Kamal et al. (1981) have made some modifications to account for the elliptical cross section and thickness variation of the parison during inflation. More recently, Cormeau et al. (1984) and Cesar de Sa (1986) considered two-dimensional inflation and cooling of annular menisci in their model of glass blowing. Unfortunately, the details of their numerical method are unclear at best, especially in the treatment of the fluid–gas and fluid–mold interaction and heat transfer. Recently, DeLorenzi and Nied (1987) have attempted a description based on a quasistatic solid analysis incorporating only normal forces due to elasticity and applied pressure. In their calculations, the pressure was increased incrementally in order to calculate progressively deformed equilibrium shapes. This idea is an extension of previous successful efforts to model the thermoforming and film blowing processes, as presented by Petrie (1983); see also references therein. However, such an analysis cannot predict the large shear stresses that initially arise in the regions of contact with the mold wall and eventually appear throughout the meniscus, or even estimate the duration of the process. Instead, Tadmor and Gogos (1979) and Petrie (1983) state that the unsteady deformation of a viscoelastic fluid should be analyzed since, in addition, the material is initially at temperatures above its "melting" point.

In contrast to previous modeling efforts, the present analysis determines the meniscus profile as part of the numerical solution by the interplay of heat transfer, pressure, viscous forces, and surface tension. It builds on our previous work providing a complete and realistic model to simulate axisymmetric and nonisothermal inflation of a meniscus confined by a cylindrical mold. However, the viscoelastic nature of the meniscus has not been accounted for, due to numerical difficulties.

Poslinski and Tsamopoulos (1991) studied isothermal inflation of a meniscus subject to values of the externally applied gas pressures that were comparable to the force of surface tension. They verified an earlier analysis of equilibrium shapes and stability of annular menisci (Tsamopoulos et al., 1988). In addition, they showed that the presence of a mold wall extended the region of parameter space where stable equilibrium shapes existed. If inertial forces were significant, oscillatory motion and fluid recirculation developed upon contact of the meniscus with the wall. Poslinski et al. (1991) extended this model to account for complications that arise during deformation driven by large values of the externally applied pressure typically encountered in industrial blow molding applications. Theoretical analysis and numerical simulations indicated that in this situation, surface tension forces became negligible except when the parison approached a mold corner, and the free meniscus was unable to achieve equilibrium until it was completely restrained by the confining mold cavity. It was also found that the instantaneous shape of the meniscus during inflation was critically affected by the magnitude of the modified Reynolds number, Re. For $Re > 1$, pressure forces became important and the flow field was similar to that in plug flow. On the other hand, if $Re < 1$, viscous forces dominated deformation, and the flow field resembled that in the laminar flow. Clearly, the different deformation history has a direct bearing on the final thickness distribution of the inflated part.

The purpose of this work is to take into account cooling and phase change effects during inflation of the meniscus and its subsequent contact with a confining mold wall. Only viscous and heat transfer effects are considered by modeling the fluid within the meniscus as a Newtonian liquid with an exponential dependence of viscosity on temperature. Inflation dynamics are governed by the momentum and energy conservation equations subject to kinematic, dynamic, and heat transfer boundary conditions. Gravitational forces are neglected since inflation occurs very rapidly in most practical applications (Tadmor and Gogos, 1979). Rather than imposing assumptions to accommodate experimentally observed parison shapes as previously done by Fukase et al. (1978), Kamal and Kalyon (1983), and others, uneven thickness variation of the parison during inflation and deformation of the material upon contact with the mold are both obtained from the solution of the proposed model.

The finite-element method is well suited for irregular and moving boundary problems. The unknown surface is either parameterized by conveniently placed spines (Kistler and Scriven, 1983; Kheshgi and Scriven, 1984), or it is described relative to a particular coordinate system (Derby and Brown, 1986; Keunings, 1986), or an elliptic mesh generation scheme is employed (Christodoulou and Scriven, 1989). Instead of this, Ettouney and Brown (1983), Tsamopoulos et al. (1985), Ungar et al. (1988), and Poslinski and Tsamopoulos (1991), among others, used nonorthogonal coordinate transformations in order to map the unknown shape to a fixed position.

An added technical difficulty of the nonisothermal inflation problem is due to solidification of the melt during its free expansion and its deformation upon contact with the cooled mold walls. Different numerical methods are available for phase change problems depending on the kind of material involved. In pure metals for example, the liquid–solid interface is sharp and corresponds to an isotherm. Thus, it may be appropriate to have part of the numerical mesh coincide with the solidification front at all times. This was employed by Ettouney and Brown (1983), Derby and Brown (1986), and Ungar et al. (1988). As an alternative, Talmon et al. (1981) and Alexandrou et al. (1989) expressed the location of the isotherms as a function of temperature and solved for the inverse problem. This method cannot be applied to problems where the isotherms have complicated shapes or are closed surfaces. For polymer melts that have a

softening zone rather than a sharp melting front, what is normally done is to include the latent heat of solidification in the heat capacity of the material, and to apply the energy conservation equation to both the solid and liquid phases. The material is considered solidified where its velocity decreases and its viscosity increases drastically (Gutfinger et al., 1975; Dantzig, 1989). In this approach, the specific heat is taken to be a continuous function of temperature, becoming strongly temperature dependent over the melting/solidification region. For example, Edwards et al. (1979) used this procedure to obtain an estimate of the cooling cycle time in blow molding operations as a function of process variables by solving the one-dimensional unsteady heat conduction equation. However, their simplified analysis does not apply to more complex forming situations. Kamal et al. (1988) also used a similar technique to incorporate heat transfer effects in their simulation of injection mold filling, although it is unclear how they accounted for the latent heat of solidification.

Due to the very short duration of meniscus inflation in blow molding and the low heat transfer coefficients from the melt to the gas, solidification is anticipated to take place after contact with the mold wall has been established. Moreover, it has been shown previously (Poslinski and Tsamopoulos, 1991) that irrespective of the applied pressure, the fluid velocity reduces to zero almost immediately in that part of the meniscus that has contacted the wall. Therefore, it should be expected that solidification will take place only in the immobile part of the meniscus. This makes unnecessary the extra complication of defining a propagating solidification front beyond which flow will be allowed.

The results obtained in the present study indicate how the inflation rate and the shape and cooling of the meniscus are determined by the interplay of temperature, pressure, and viscous forces. In addition, the transient calculations illustrate how the computer simulation may be used to improve design of blow molding operations, and to predict inflation times and thickness distribution of the final product as a function of the material properties, process conditions, and mold configuration. The results are important for development of a realistic simulation and optimization of blow molding for even more complicated parts, as well as other related polymer processing operations. Governing equations and boundary conditions that describe deformation and cooling of the meniscus are presented in the next section. Following that, finite-element numerical solution techniques are summarized. Then inflation of the meniscus within a cylindrical mold cavity is analyzed, and the computer simulations are compared with available experiments. Finally, a summary and pertinent conclusions are given.

Nonisothermal Inflation Model

Figure 2 shows a cross section of a liquid annular meniscus pinched at both ends within a cylindrical mold cavity of radius $\tilde{R}_w$ and length $\tilde{L}$. Motion of material held between the confining walls is neglected, and it is assumed that the liquid forms two fixed, concentric and circular contact lines. The outer contact line has a radius $\tilde{r}_o$ and the inner one, $\tilde{r}_o - \tilde{\delta}_o$, where $\tilde{\delta}_o$ is the thickness of the gap at the upper and lower mold walls. By applying a pressure gradient $\tilde{P}_I - \tilde{P}_o$ across the two gas–liquid interfaces, the meniscus inflates from its initial annular shape with an axisymmetric profile that depends on time. During deformation, the gas temperature $\tilde{T}_G$ and wall temperature $\tilde{T}_w$ are assumed to be constant. The inner and outer gas–liquid

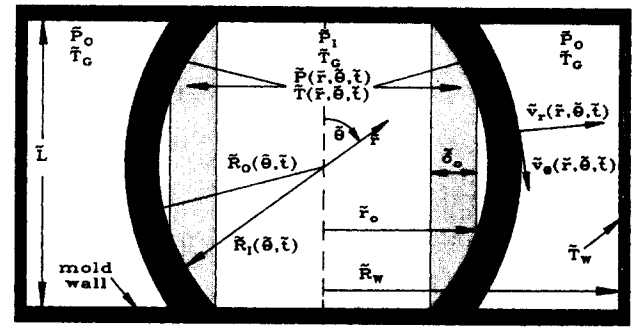

Figure 2. Cross section of annular meniscus defined relative to a spherical coordinate system ($\tilde{r}$, θ).

surfaces are given by $\tilde{r} = \tilde{R}_I(\theta, \tilde{t})$ and $\tilde{r} = \tilde{R}_o(\theta, \tilde{t})$ in the Mongé representation relative to a spherical coordinate system $(\tilde{r}, \theta)$ centered at the midplane of the meniscus. The fluid temperature and pressure are denoted as $\tilde{T}(\tilde{r}, \theta, \tilde{t})$ and $\tilde{P}(\tilde{r}, \theta, \tilde{t})$; the radial and axial velocities are given by $v_r(\tilde{r}, \theta, \tilde{t})$ and $v_\theta(\tilde{r}, \theta, \tilde{t})$, respectively.

For an incompressible viscous fluid, the dimensionless form of the mass, momentum, and energy conservation equations neglecting gravitational forces are:

$$\nabla \cdot \boldsymbol{v} = 0 \tag{1}$$

$$Re\left(\frac{\partial \boldsymbol{v}}{\partial t} + \boldsymbol{v} \cdot \nabla \boldsymbol{v}\right) = -\nabla \cdot \sigma \tag{2}$$

$$Pe\, C_p(T)\left(\frac{\partial T}{\partial t} + \boldsymbol{v} \cdot \nabla T\right) = \nabla^2 T - Br\sigma : \nabla \boldsymbol{v} \tag{3}$$

where Re, Pe, and Br are the Reynolds, Peclet, and Brinkman numbers, respectively, and the total stress is defined as $\sigma = PI - \mu(T)\,(\nabla \boldsymbol{v} + \nabla \boldsymbol{v}^T)$. The specific heat and viscosity functions, $C_p(T)$ and $\mu(T)$, are scaled with the appropriate values C_p^o and μ_o, respectively, evaluated at the reference temperature of the material, $\tilde{T}_o$. Variables are made dimensionless with the characteristic pressure drop $\Delta\tilde{P}$, temperature difference $(\tilde{T}_o - \tilde{T}_w)$, and length $\tilde{r}_o$. Table 1 lists the relevant dimensionless groups that arise in this model. The energy conservation equation is applied to both solid and liquid phases. The latent heat of solidification has been incorporated in the specific heat, which is a continuous function of temperature as shown in Figure 3 for high-density polyethylene (HDPE) (Tadmor and Gogos, 1979). For computational convenience the

Table 1. Dimensionless Groups in the Nonisothermal Inflation Model.

Reynolds no.	$Re = (\rho \tilde{r}_o^2 \Delta\tilde{P})/(\mu_o^2)$
Peclet no.	$Pe = (\rho C_p^o \tilde{r}_o^2 \Delta\tilde{P})/(\mu_o k)$
Brinkman no.	$Br = (\tilde{r}_o^2 \Delta\tilde{P}^2)/(\mu_o k)/(\tilde{T}_o - \tilde{T}_w)$
Pressure drop parameter	$\Delta P = (\tilde{r}_o \Delta\tilde{P})/\gamma$
Biot no., for surface j	$Bi_j = (\tilde{r}_o U_j)/k$
Viscosity ratio	$\mu(T) = \tilde{\mu}(\tilde{T})/\mu_o$
Specific heat ratio	$C_p(T) = \tilde{C}_p(\tilde{T})/C_p^o$
Aspect ratio	$\alpha = \tilde{r}_o/\tilde{L}$
Contact thickness ratio	$\delta = \tilde{\delta}_o/\tilde{r}_o$

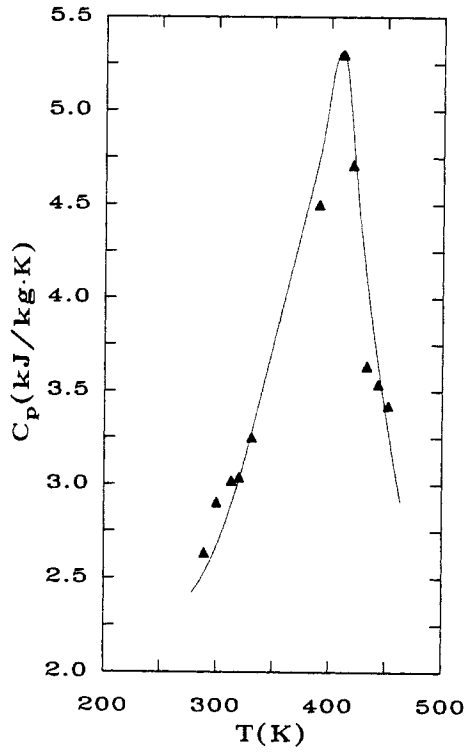

Figure 3. Dependence of specific heat capacity on temperature for high-density polyethylene.

experimental points for temperatures between 275 and 470 K were fitted by six polynomials that were piecewise continuous and had continuous first derivatives (Poslinski, 1990). The following Arrhenius dependence was found to fit the viscosity data for HDPE very well in the temperature range of $275 < T < 500$ K:

$$\tilde{\mu} \equiv \mu_o \exp\left[1{,}432\left(\frac{1}{\tilde{T}} - \frac{1}{\tilde{T}_o}\right)\right]. \tag{3a}$$

The experimental values of viscosity were determined using temperature shift factors (Bird et al., 1987). The temperature variation of density, thermal conductivity, and surface tension is less significant and these properties are assumed to be constant. Table 2 lists the thermophysical properties of HDPE at a reference temperature of 413 K. Although the treatment at this stage only considers a specific material, it can readily be extended to deal with other materials as well.

Appropriate boundary conditions are required on every portion of the parison boundary. At the inner and outer fluid interfaces, a local normal force balance between viscous stress,

Table 2. Thermophysical Properties of HDPE at Ref. Temp. $\tilde{T}_o = 413$ K

Property	Value	Ref.
ρ	780 kg/m^3	Bird et al. (1987)
k	0.26 W/m · K	Bird et al. (1987)
γ	0.028 N/m	Wu (1974)
μ_o	2.4 kPa · s	Tanner (1985)
C_p^o	5.2 kJ/kg · K	Tadmor and Gogos (1979)

surface tension, and gaseous pressure results in the following dynamic conditions:

$$\boldsymbol{n}_I \cdot \boldsymbol{\sigma}|_{r=R_I} = \frac{(P_I + 2\mathcal{H}_I)\boldsymbol{n}_I}{\Delta P} \tag{4a}$$

$$\boldsymbol{n}_o \cdot \boldsymbol{\sigma}|_{r=R_o} = \frac{(P_o - 2\mathcal{H}_o)\boldsymbol{n}_o}{\Delta P} \tag{4b}$$

The outer gas pressure, P_o, is set to the atmospheric pressure as the pressure datum. The inner pressure, P_I, is taken as the sum of the pressure required to balance the surface tension forces in order to maintain a perfect annular shape, plus the additional pressure drop, ΔP, that causes the annulus to deform. Increasing or decreasing ΔP from zero corresponds to inflation or deflation from the initial shape, respectively. As a result of the chosen scalings, the pressure drop parameter plays the role of the capillary number that usually arises in the dynamic conditions, Eqs. 4a and 4b. Indeed, for large values of ΔP, surface tension forces during deformation become negligible except when the parison approaches a mold corner, which results in a very small radius of curvature; see Poslinski et al. (1991) for further details.

Two other boundary conditions arise at the free surfaces as a result of kinematic principles and heat transfer considerations. Written for each surface, the first condition, equates the velocity of the moving boundary to the fluid velocity:

$$\boldsymbol{n}_I \cdot \left(\frac{\partial R_I}{\partial t}\boldsymbol{e}_r\right) = \boldsymbol{n}_I \cdot \boldsymbol{v}|_{r=R_I} \tag{5a}$$

$$\boldsymbol{n}_o \cdot \left(\frac{\partial R_o}{\partial t}\boldsymbol{e}_r\right) = \boldsymbol{n}_o \cdot \boldsymbol{v}|_{r=R_o} \tag{5b}$$

The second condition describes the convective heat loss to the surroundings:

$$\boldsymbol{n}_I \cdot \nabla T = Bi_I(T - T_G) \tag{6a}$$

$$-\boldsymbol{n}_o \nabla T = Bi_o(T - T_G), \tag{6b}$$

where $\boldsymbol{n}_{I,o}$ are unit vectors normal to either surface in the positive radial direction. In Eqs. 6a and 6b, the magnitude of the Biot numbers, $Bi_{I,o}$, depends on the estimation of the heat transfer coefficient $U_{I,o}$. The heat transfer coefficient is affected by the gas conductivity and, as a result, is significantly higher at the inner surface due to the larger gaseous pressure (Poslinski, 1990). Furthermore, forced convection reduces to natural convection upon cessation of flow in that part of the meniscus that has contacted the confining mold walls. By treating each material point on the gas–liquid interface as a point of stagnation flow, the upper bound of the heat transfer coefficient for forced convection, h_{fj}, can be obtained with the aid of boundary-layer theory (Schlichting, 1979). It can be shown that h_{fj} is proportional to the square root of the normal free-surface velocity, and it depends on the Prandtl number of the gas. Similarly, the heat transfer coefficient for natural convection,

h_{nj}, depends on the Prandtl and Grashof numbers. Thus,

$$U_j = \begin{cases} h_{fj}\sqrt{(\boldsymbol{n}_j \cdot \boldsymbol{v})}|_{r=R_j}, & U_j > h_{nj} \\ h_{nj}, & \text{otherwise.} \end{cases} \tag{7}$$

Table 3 lists estimated values of these constants for several different values of the applied pressure, taking air to be the cooling medium. For further details see Poslinski (1990).

Prior to inflation, the meniscus is most often produced by extrusion using a reciprocating screw device or by injection. Thus, the temperature of the material that extends past the mold surfaces may be higher than the temperature of the cooled walls. In order to investigate the importance of this effect, the temperature of the material at the upper contact surface may be assumed to be governed by the one-dimensional energy balance,

$$Pe\,C_P(T)\frac{\partial T}{\partial t} = \frac{\partial^2 T}{\partial r^2} + \frac{1}{r}\frac{\partial T}{\partial r} \tag{8}$$

with boundary conditions,

$$r = 1, 1 - \delta \qquad T = 0 \tag{9a}$$

$$t = 0 \qquad T = T_u \tag{9b}$$

Equations 8 and 9 describe the unsteady radial heat flow in an infinite annulus of inner radius $1 - \delta$ and outer radius 1. The initial temperature at the upper boundary, T_u, provides the flexibility of setting an appropriate constant temperature level prior to inflation. Setting T_u to zero indicates that the material confined between the two mold walls has solidified and cooled to the mold wall temperature prior to inflation, that is, $\tilde{T}_u = \tilde{T}_w$. In the other extreme, a value of unity implies that the confined liquid has not been cooled prior to inflation, $\tilde{T}_u = \tilde{T}_o$.

An equilibrium analysis between pressure and surface tension forces on an annular meniscus (Tsamopoulos et al., 1988) revealed, among other things, that in the absence of gravity, disturbances in the externally applied pressure resulted in meniscus shapes that were reflectively symmetric with respect to the $z = 0$ plane. Consequently, only a quadrant of the entire meniscus profile is considered, and at the midplane, boundary conditions due to symmetry are imposed:

$$v_\theta = 0, \sigma_{r\theta} = 0, \frac{\partial T}{\partial \theta} = 0, \frac{\partial R_j}{\partial \theta} = 0 \quad \text{at} \quad \theta = \pi/2. \tag{10}$$

At the upper contact surface, experimental observations indicate that the meniscus forms two static attachment lines with the mold walls (Kamal et al., 1981). Consequently, the condition of no-slip is imposed there and the location of the contact lines is fixed as follows:

$$R_I = \frac{1}{(2\alpha \cos\theta_I)} \tag{11a}$$

$$R_0 = \frac{1}{(2\alpha \cos\theta_o)} \tag{11b}$$

with angular positions,

$$\theta_I = \arctan\,[2\alpha(1 - \delta)] \tag{12a}$$

$$\theta_o = \arctan\,[2\alpha]. \tag{12b}$$

The radial location of both confining walls relative to the spherical coordinate system is obtained from geometrical considerations and is given by Poslinski (1990). As the meniscus contacts solid surfaces during confined inflation, temperature and location of the outer gas–liquid interface are fixed to the temperature and radius of the mold wall, respectively, and no-slip is imposed thereafter. Once the outer surface makes contact, it is not allowed to detach from the wall; however, the inner surface is free to deform further during the impingement process. Application of no-slip at the dynamic contact line between meniscus and solid surfaces is appropriate when viscous forces dominate surface tension effects (Kistler and Scriven, 1983; Behrens et al., 1987, 1988). This is the case in blow molding operations. Otherwise, surface forces at the dynamic contact line require a more careful assessment as discussed in the review by Dussan (1979) and in Poslinski and Tsamopoulos (1991).

To close the set of Eqs. 1–12, appropriate initial conditions are required. Calculations start from a perfectly annular shape such that the velocity field is identically zero and the fluid pressure assumes a hydrostatic value of ΔP^{-1}, in addition to the outer gaseous pressure. The external pressure is imposed as either a step change in the inner gas pressure, or a linear increase over a short time interval similar to the practice in blow molding. In general, other initial configurations of the meniscus can be examined as has been done by Poslinski et al. (1991). The temperature field may be taken either to be initially uniform, or to follow a distribution dictated by natural cooling or other meniscus history prior to inflation.

Table 3. Heat Transfer Coefficients for Natural and Forced Convection as a Function of Applied Pressure Drop

$\Delta\tilde{P}$ kPa	h_{no}* W/m² · K	h_{ni}** W/m² · K	h_{fo}* W/m² · K	h_{fi}** W/m² · K
68.95	8	10	50	65
344.75	8	14	140	300
758.45	8	26	210	620
1,034.25	8	31	240	810

*At outer free surface and atmospheric pressure
**At inner free surface taking into account increased pressure

Numerical Solution Technique

The governing equations, Eqs. 1–3, were solved by including heat transfer and phase change effects in the transient finite-element algorithm developed by Poslinski and Tsamopoulos (1991) and Poslinski et al. (1991). Very briefly, the method combines Galerkin/finite-element discretization coupled with a fully implicit, variable time step algorithm (Gresho et al., 1983; Kheshgi and Scriven, 1984) with significant modifications to account for complications arising when the meniscus interacts with the confining mold walls; see Poslinski (1990) for a more complete description. The numerical scheme determines simultaneously the flow field and temperature distribution within the meniscus together with the moving-surface location at every time step. In order to take into account the changing flow domain during inflation, the weighted residual equations are

transformed from the physical coordinate system (r, θ, t) to a computational coordinate system, (η, ξ, τ) by the following mapping:

$$\eta = 1 + \delta\left[\frac{r - R_0(\theta, t)}{R_0(\theta, t) - R_l(\theta, t)}\right] \tag{13a}$$

$$\xi = \theta \tag{13b}$$

$$\tau = t \tag{13c}$$

for $\theta_o \le \theta \le \pi/2$. As shown in Figure 4, the physical domain in the region $\theta_l \le \theta \le \theta_o$ is bounded by the upper mold surface, R_u, which corresponds to the curve η_u in the computational domain. The appropriate transformation in this region is

$$\eta = (1 - \delta) + [\eta_u(\theta) - (1 - \delta)]\left[\frac{r - R_l(\theta, t)}{R_u(\theta) - R_l(\theta, t)}\right] \tag{14a}$$

$$\xi = \theta \tag{14b}$$

$$\tau = t \tag{14c}$$

where

$$R_u(\theta) = \frac{1}{(2\alpha \cos\theta)} \tag{15a}$$

$$\eta_u(\theta) = \frac{(1 - \delta)\sin(\theta_o - \theta_l)}{\sin(\theta_o - \theta) + (1 - \delta)\sin(\theta - \theta_l)} \tag{15b}$$

The overall transformation effectively maps the deformed meniscus back to a fixed domain that is described by a segment of a spherical shell of outer radius equal to unity and thickness δ. The computational domain that accounts for a quadrant of the entire meniscus profile is discretized into a finite-element mesh. For velocity and temperature, nine-node isoparametric rectangular elements are used in the bulk of the domain and six-node triangular elements are used near the upper contact surface (Strang and Fix, 1973). The pressure field is approximated by bilinear elements and three-node triangular elements in the respective domains. Finally, the inner and outer gas–liquid interfaces are discretized by Lagrangian quadratic basis. The grid is defined at the start of the transient integration, and due to the mapping the necessity of numerically tracking deforming elements in the physical domain is avoided. The mapping, however, adds to the complexity of the formulation by introducing new spatial and time derivatives into the governing equations, as explained by Poslinski and Tsamopoulos (1991).

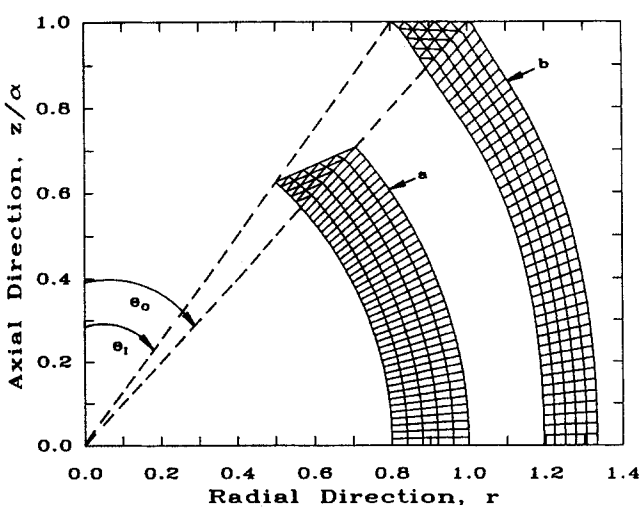

Figure 4. Finite-element mesh used for calculating meniscus shapes.

(*a*) computational domain (η, ξ); (*b*) physical domain (r, θ)

The finite-element representations of the unknown variables are given by:

$$v(\eta, \xi, \tau) = \sum_i v^i(\tau)\phi^i(\eta, \xi) \tag{16a}$$

$$T(\eta, \xi, \tau) = \sum_i T^i(\tau)\phi^i(\eta, \xi) \tag{16b}$$

$$P(\eta, \xi, \tau) = \sum_i P^i(\tau)\psi^i(\eta, \xi) \tag{16c}$$

$$R_j(\eta, \xi, \tau) = \sum_i R_j^i(\tau)x^i(\xi) \tag{16d}$$

where (v^i, T^i, P^i, R_j^i) are the unknown nodal variables, $x^i(\xi)$, $\phi^i(\eta, \xi)$, and $\psi^i(\eta, \xi)$ are the basis functions, and j corresponds to either the inner or outer surface. Written in the physical domain first, the weak form of the continuity, motion, energy, and kinematic equations used to determine pressure, velocity, temperature, and surface locations, respectively, are as follows:

$$\int_V \psi^i \nabla \cdot v\, dV = 0 \tag{17}$$

$$\int_V \left[Re\phi^i\left(e_k \cdot \frac{Dv}{Dt}\right) - \nabla(\phi^i e_k):\sigma\right] dV + \int_{S_o} (\phi^i e_k)n_0:\sigma\, dS_o - \int_{S_l} (\phi^i e_k)n_l:\sigma\, dS_l = 0 \tag{18}$$

$$\int_V \left\{\phi^i\left[PeC_P(T)\frac{DT}{Dt} + Br\,\sigma:\nabla v\right] + \nabla\phi^i \cdot \nabla T\right\} dV - \int_{S_o} [\phi^i n_o \cdot \nabla T]\, dS_o + \int_{S_l} [\phi^i n_l \cdot \nabla T]\, dS_l = 0 \tag{19}$$

$$\int_{S_j}\left[x^j n_j \cdot \left(\frac{\partial R_j}{\partial t}e_r - v\right)\right] dS_j = 0 \tag{20}$$

where $dV = r^2 \sin\theta dr d\theta$ and $dS_j = R_j^2[1 + (1/R_j\, \partial R_j/\partial\theta)^2]^{1/2} \sin\theta d\theta$ denote the differential unit volume and surface areas, respectively. The subscript k represents the two components of the momentum equations (r, θ); e_k designates the corresponding unit base vectors; and D/Dt is the material derivative. The divergence theorem has been used in the momentum and energy equations to reduce continuity requirements on the basis functions ϕ^i, and the dynamic and heat transfer boundary conditions, Eqs. 4 and 6, are applied by direct substitution in the surface integrals of the respective residuals. In addition, continuity requirements on the free-surface basis functions x^i are reduced

by invoking the surface divergence theorem on the boundary terms in Eq. 18 after using a convenient expression for the surface curvature term, $2\mathcal{H}$ (Keunings, 1986; Poslinski and Tsamopoulos, 1991).

At every time step, the algorithm simultaneously solves the nonlinear system of algebraic equations using modified Newton iterations. Convergence is achieved when the Euclidian norm, $\|\boldsymbol{u}^{(k+1)} - \boldsymbol{u}^{(k)}\|_2$ of all the unknowns, $\boldsymbol{u}^t = (\boldsymbol{v}^{it}, T^i, P^i, R_j^i)$, falls below the specified tolerance of 10^{-9}. This conservative requirement is imposed to ensure high accuracy in determining the free-surface shape, which is of main interest for the problem studied here. The linear equation set at each iteration is solved by direct LU factorization accounting for the arrowlike structure of the Jacobian matrix (Thomas and Brown, 1987). The number of radial elements in the mesh is crucial to the resolution of temperature gradients encountered during confined inflation. As verified by Poslinski (1990), the solution during the entire inflation process is resolved by using seven radial and 40 axial rectangular elements and 49 triangular elements for a total of 329 elements and 4,492 unknowns. A smaller mesh of 5 by 40 is shown in Figure 4 for clarity. The calculations were performed using the IBM 3090 Supercomputer Facility at Cornell University. The code was optimized as discussed in Poslinski et al. (1991), and demonstrated in Poslinski (1990). It required four to five iterations per time step, and 500 to 600 time steps for the meniscus to completely fill the mold cavity and cool to the surrounding gas temperature. This amounts to approximately between 90 and 100 CPU hours per computation.

Numerical Results

In the following subsections, the nonisothermal model is used to analyze inflation dynamics and heat transfer during free and confined inflation of an annular parison using the thermophysical properties of high-density polyethylene. It is not feasible to give in this paper the wealth of information provided by the present methodology, instead we will focus on variables and effects of primary relevance only. Table 4 lists the values of the dimensionless groups that are typical under blow molding conditions and are used in the simulations. The characteristic radius that corresponds to case A and case B was chosen to be 1 and 1.225 cm, respectively, typical of small-volume bottle applications. The values for case B are also used to compare the numerical results with available experiments. The Reynolds number in both cases is much smaller than unity, indicating that viscous forces dominate. In addition, the high values of the Peclet number arise as a result of the low thermal conductivity of polymer melts; in comparison, viscous heating as measured by the Brinkman number is less significant. Inspection of Table 1 reveals that *Re*, *Pe*, and *Br* are all expressed in terms of the externally applied pressure, and *Bi* depends on the total pressure through the physical properties of the cooling gas. In order to examine the effect of the operating pressure and to simulate industrial conditions as closely as possible, $\Delta\tilde{P}$ was varied from 10 to 110 psi (69 to 1,034 kPa). This variation results in an order of magnitude increase in the dimensionless groups from case A to B. The mold wall and ambient gas temperatures for all transient calculations were set to $\tilde{T}_w = 283$ K and $\tilde{T}_G = 293$ K. In the following subsection, nonisothermal inflation into a mold cavity characterized by a 90° mold corner is analyzed, elucidating the interplay of heat transfer and solidification during deformation. The effect of variation in the fluid temperature prior to inflation on the instantaneous shape of the parison and final thickness distribution is given in the following second subsection, and computer simulations are compared to available experiments in the third subsection.

Table 4. Values of Dimensionless Groups Used in Simulations

Parameter	Case A	Case B
Re	0.001	0.015
Pe	4×10^4	7.5×10^5
Br	5.0	1×10^3
ΔP	2×10^4	3×10^5
Bi_{fl}	2.5	28
Bi_{fo}	2.0	10
Bi_{nl}	0.4	1.2
Bi_{no}	0.3	0.3
α	0.25	0.1
δ	0.2	0.3
R_w	2.0	2.0
t_o	0.0	70.0

Inflation into a 90° mold corner

Figure 5 shows the instantaneous shapes for a quadrant of the entire meniscus profile during confined inflation into a 90° mold corner using parameters for case A. The initial meniscus temperature is taken to be uniform throughout the meniscus, that is, $T = 1$ ($\tilde{T} = 413$ K) except at the upper contact surface, where it is first set to the mold wall temperature, $T_u = 0$

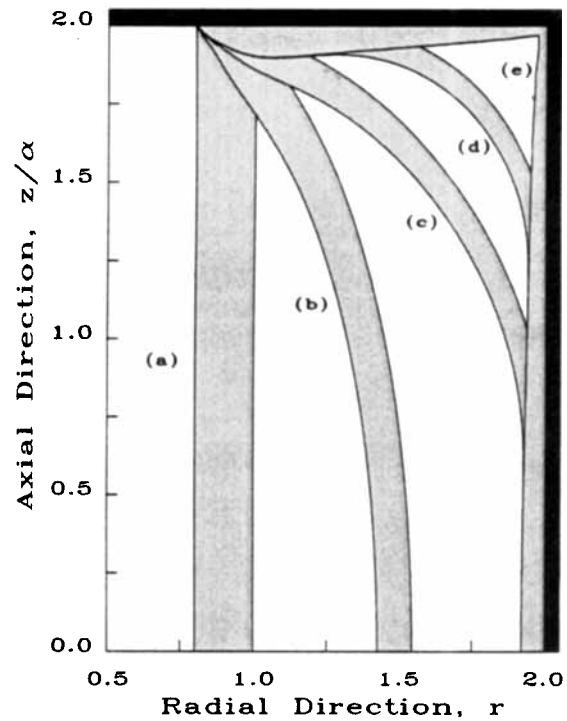

Figure 5. Instantaneous shapes of annular meniscus during confined inflation into a 90° mold corner.

Case A, $T_u = 0$
(*a*) $t = 0.0$; (*b*) $t = 0.2908$; (*c*) $t = 0.4272$
(*d*) $t = 0.5170$; (*e*) $t = 5.002$

($\tilde{T}$ = 283 K). As discussed in the previous section, this condition implies that the material past the upper confining solid surfaces has solidified prior to inflation. The results are plotted relative to a cylindrical coordinate system (r, z) where a radial distance of $r = 0$ corresponds to the axis of symmetry and an axial distance of $z/\alpha = 0$ to the midplane of the meniscus. The applied pressure drop, $\Delta P = 2 \times 10^4$ (10 psi), is imposed as a step change in the inner gas pressure. Figure 5 indicates that the meniscus inflates from its initial annular shape with a profile of nonuniform thickness that resembles an ellipse. The meniscus doubles in diameter before it contacts the mold surface at the midplane first, and it becomes progressively thinner as it approaches the mold corner. An equilibrium shape is not achieved until full contact with the mold cavity has been established. The inflation cycle resulting in full attachment of the meniscus to the confining mold surface is completed very quickly, within a dimensionless time of 5.002, which under these conditions corresponds to approximately 0.174 s.

Figure 6 shows the time evolution of the temperature at three different locations on the midplane of the meniscus during free and confined inflation: the inner surface, the outer surface, and the midpoint between them. During free inflation, the inner and outer gas–liquid interfaces are slightly cooled due to forced convection; whereas the temperature in the bulk of the meniscus exhibits inappreciable heating due to viscous dissipation. The higher heat transfer coefficient at the inner surface results in lower temperature there, in comparison to the temperature at the outer surface. Variations in the estimated values of the heat transfer coefficient or heating of the air did not affect these results. As the meniscus makes contact with the mold at t = 0.3954 (0.0138 s), the temperature at the outer surface is set to the mold wall temperature. This high rate of cooling in the outer surface could freeze-in the instantaneous molecular orientations of the polymer, whereas the slower cooling rates toward the inner surface could allow for stress relaxation to take place. The resulting variations in degrees of crystallinity have been observed experimentally by Kamal and Kalyon (1983). Due to the simultaneous and sudden reduction in the normal component of surface velocity, forced convection in the midplane switches to natural convection. As a result, the value of the heat transfer coefficient at the inner surface is significantly decreased. Subsequently, the temperature at the inner surface is slightly increased because of the combination of the new lower rate of heat removal from there and the sustained heat flow from the middle of the meniscus. The temperature in the bulk remains almost unchanged during these initial stages of impingement.

Figure 7 shows the temperature profiles calculated at the midplane after the meniscus has made partial contact with both mold walls. The usual thermal boundary layer develops near the cold wall. This figure also demonstrates that insignificant cooling takes place through the inner surface due to convection to the gas. Instead, the bulk of heat losses are due to conduction to the wall. The fluid temperature at the midplane approaches the wall temperature by a dimensionless time of 46 (1.6 s).

A close-up of the contact region, Figure 8a, indicates that the velocity is dramatically reduced there. Therefore, only the subsequent movement toward the wall of material downstream from the contact region results in the apparent motion of the contact line, and not the displacement of material by the almost stagnant fluid upstream. Transient fluid recirculation zones near the contact line that were previously found (Poslinski and Tsamopoulos, 1991) are not observed. This should be expected because the Re number in the present calculations is much smaller than unity. The pressure distribution at the same point in time, t = 0.4271 (0.0148 s), shows that the remaining free meniscus is undergoing extension, Figure 8b, whereas upstream from the contact line the total stress quickly relaxes and approaches the hydrostatic value of unity.

Fluid velocity and temperature isotherms at t = 0.4640

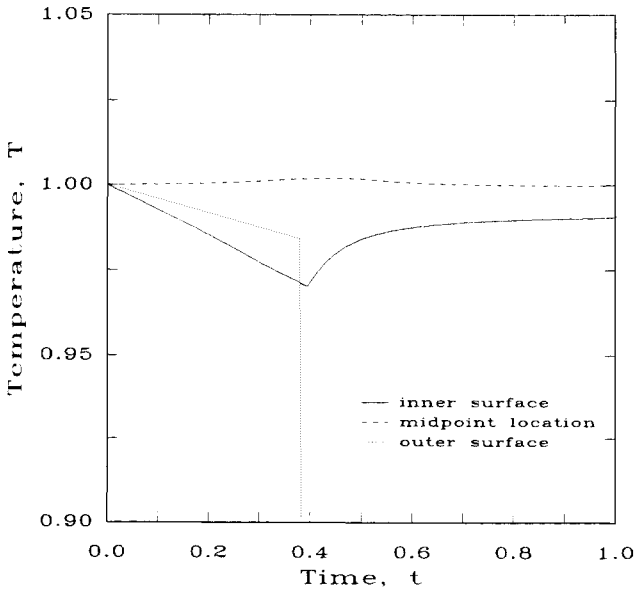

Figure 6. Time evolution of temperature at three locations along midplane of meniscus during initial stages of impingement process.

Case A, $T_u = 0$

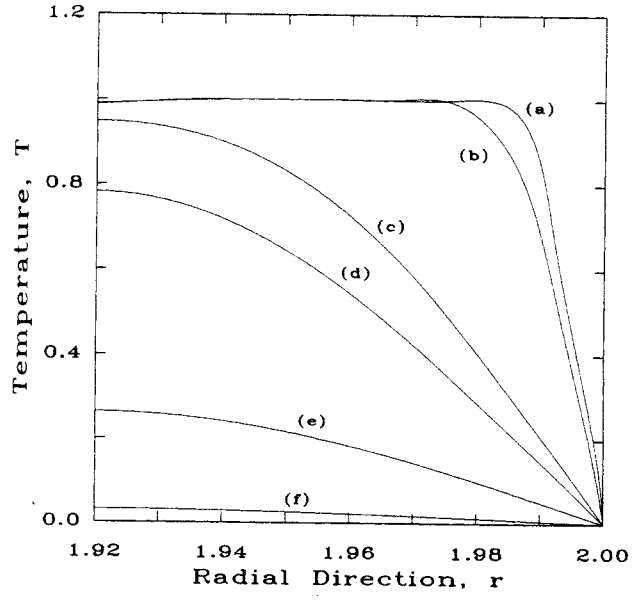

Figure 7. Temperature profiles at midplane during confined inflation.

Case A, $T_u = 0$
(*a*) t = 0.590; (*b*) t = 0.752; (*c*) t = 5.0
(*d*) t = 9.21; (*e*) t = 23.8; (*f*) t = 45.9

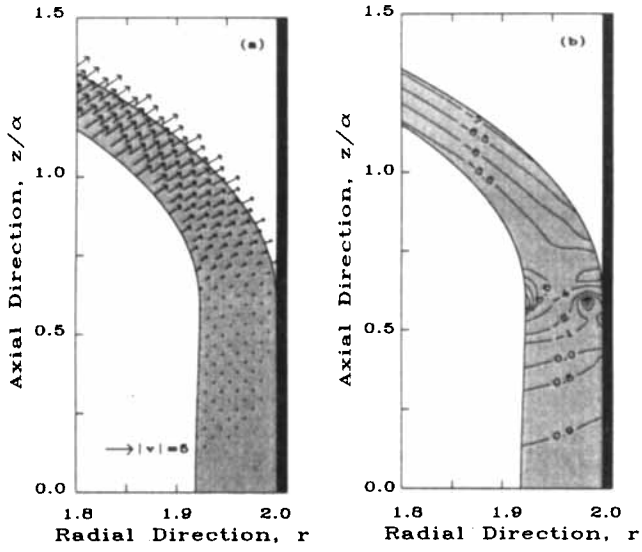

Figure 8. Close-ups during impingement process at t = 0.4271.

Case A, $T_u = 0$
a. Velocity profile
b. Pressure profile

(0.0161 s) are shown in Figure 9. Most of the parison is still at the original dimensionless temperature of 1. Close comparison of Figures 9a and 9b provides full justification of the present model, which does not explicitly account for the solidification front. In general, the solidification front not only divides a pure material into solid and molten phases, it is also the surface beyond which heat transfer by convection may or may not take place. The former effect results in discontinuities in the thermophysical properties and the heat flux through the front; the latter effect implies that a different form of the energy conservation equations must be solved for each phase. However, in the present physical problem this is not necessary because flow has ceased prior to the formation and ahead of the solidification front.

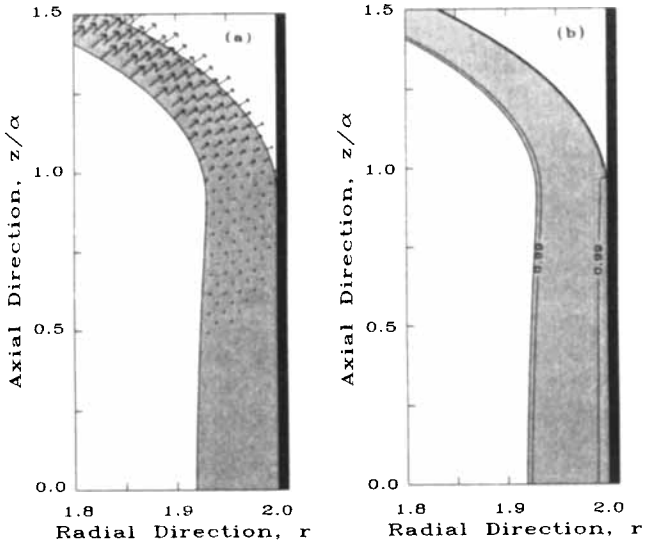

Figure 9. Close-ups during inflation at t = 0.4640.

a. Velocity profile.
b. Temperature isotherms

Indeed, if the material is considered solidified at the temperature where its viscosity increases by one order of magnitude from the original value, then it is solidlike for a radial distance of 0.003 from the mold wall, or 3.6% of its thickness. At the same time and for all practical purposes flow has already ceased at all radial locations of that part of the parison that has contacted the wall. Figure 9 also makes plain that motion of the parison stops not because it has solidified, as was conjectured in the literature (Ryan and Dutta, 1982), but because of its contact with the mold wall.

A close-up of the temperature distribution at a much later point in time, t = 9.21 (0.320 s), reveals that the meniscus has now practically cooled to the mold wall temperature, Figure 10. Although the temperature in the upper contact surface is set to the wall temperature, the hottest material remains near the upper mold wall, where the inflated part is observed to be thicker. Cooling of the meniscus is achieved by heat conduction to the mold surfaces in both the radial and axial directions. Consequently, the isotherms are not necessarily parallel to the mold walls and the inner gas–liquid boundary does not correspond to an isotherm, in contrast to predictions of the earlier one-dimensional models (Edwards et al., 1979, and others). This temperature variation on the parison surface is not sufficient to initiate thermocapillary convection due to surface tension gradients, since the Marangoni number is here much less than one, given that $-(\partial\gamma/\partial T) = 6.7 \times 10^{-5}$ N/m · K (Wu, 1974). The entire cooling cycle required approximately 2.12 s (t = 61) to reduce the temperature level to the ambient gas temperature. Inflation of the meniscus takes only a small percentage of the cooling time, less than 10% in the present case A.

In the next simulation, the temperature at the upper contact surface was allowed to vary according to Eq. 8, starting from the uniform value of T_u = 1. In contrast to the previous case, this temperature level implies that the material past the upper mold surface has not cooled down at all prior to inflation. As shown in Figure 11, the usual thermal boundary layer initially develops

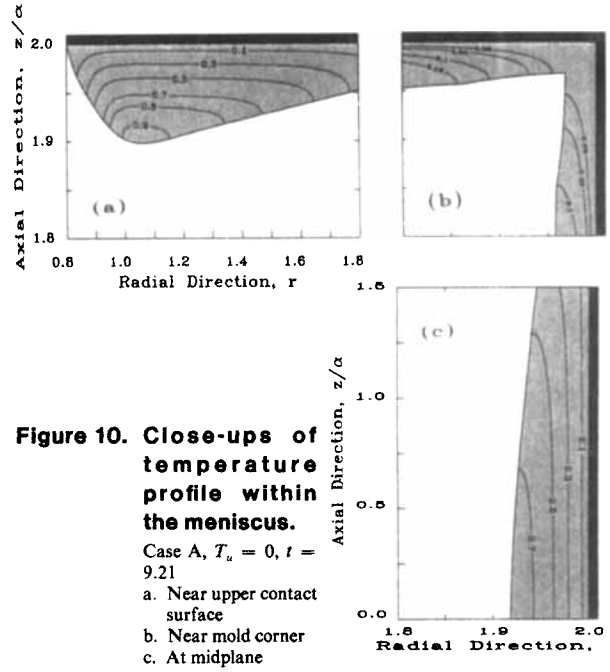

Figure 10. Close-ups of temperature profile within the meniscus.

Case A, $T_u = 0$, t = 9.21
a. Near upper contact surface
b. Near mold corner
c. At midplane

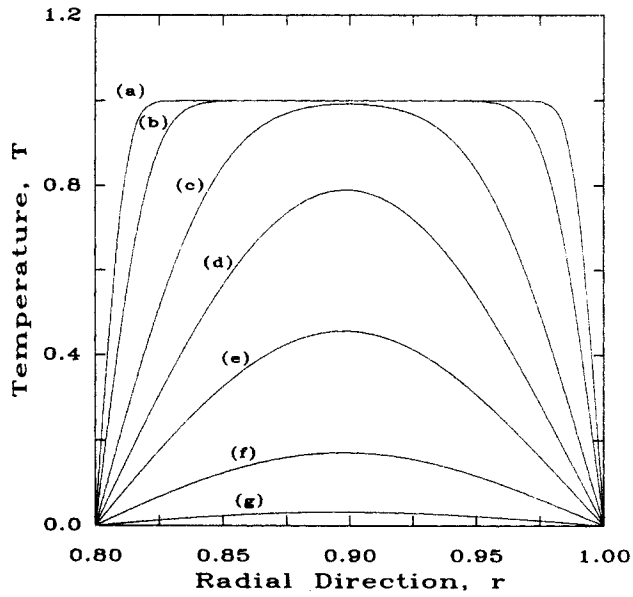

Figure 11. Temperature profiles imposed at upper contact surface of meniscus.

Case A, $T_u = 1$
(*a*) $t = 0.3056$; (*b*) $t = 1.019$; (*c*) $t = 5.122$; (*d*) $t = 15.43$
(*e*) $t = 30.14$; (*f*) $t = 50.17$; (*g*) $t = 80.16$

near the walls. Subsequently, the temperature approaches the wall temperature by a dimensionless time of 80 (2.78 s), long after the meniscus had filled the mold cavity. Imposition of this time-dependent boundary condition on temperature, however, only affects the deformation process very close to the upper surface of the mold. Meniscus shapes and inflation rate obtained starting with this initial condition are virtually the same as those shown in Figure 5, where $T_u = 0$ was used (Poslinski, 1990).

Variation of initial temperature in the bulk of the parison

It is of interest to investigate how the initial temperature level as well as temperature distribution within the meniscus affect the inflation dynamics and the final thickness distribution of the blown part. In blow molding, a temperature distribution may arise during the formation of the meniscus and uneven cooling of the material prior to inflation. Complicated equipment configuration and short cycle times make it difficult to determine accurately the initial temperature distribution. Haessly (1989) measured surface temperatures approximately by stopping production and using a pyrometer. He, as well as DeLorenzi and Nied (1987), found that for injection blow molding the meniscus is cooler in the vicinity of the upper mold surface prior to inflation.

Computer simulations using parameters for case A were carried out starting with two different temperature distributions. The first distribution was obtained by cooling the meniscus from an initial uniform temperature of $T = 1$ (413 K) for up to $t = 90$ prior to inflation. Heat was lost at the upper contact surface, where Eq. 8 was employed, and through natural convection at the inner and outer parison interfaces. This resulted in reduced temperatures close to the static attachment lines, whereas the temperature in the bulk of the meniscus remained virtually unchanged (Poslinski, 1990). The second initial temperature distribution is closer to Haessly's (1989) measurements. The following quadratic expression was found to fit his data adequately:

$$T = (T_M - T_u)[1 - (2\alpha r \cos\theta)^2] + T_u. \qquad (18)$$

Equation 18 describes an initial temperature distribution that increases axially from $T = T_u$ at the upper contact surface to a maximum value $T = T_M$ at the midplane.

Table 5 lists the dimensionless inflation time to reach the mold wall at the midplane, t_R, the time to completely fill the mold cavity, t_c, and the thickness of the inflated part at the midplane and at the end of the inflation cycle, δ_w. Real times can be calculated by multiplying the respective dimensionless values by the characteristic ratio $(\mu_o/\Delta\tilde{P})$ of 0.0348 s. The temperature level in the quadratic profiles was adjusted by varying the maximum temperature between $1 \le T_M \le 1.4$ ($413 \le \tilde{T}_M \le 465$ K). Results indicate that by increasing the temperature, the inflation rate is increased due to reduced viscosity; however, the final thickness is virtually unaffected (Poslinski, 1990). It is interesting to note that the higher temperatures increase the cooling rate through the wall and approximately 1.42 s are required to reduce the midplane temperature at the inner surface to the wall temperature for all three cases studied.

Figure 12 illustrates the final thickness distribution of the inflated meniscus obtained using the various temperature profiles. The results acquired with the isothermal model (Poslinski et al., 1991) are also shown for comparison. The dimensionless thickness δ_w is calculated normal to the mold surface, and the wall perimeter distance s is measured along the periphery of the inner mold wall. In particular, the values of $s = 0$, 2, and 3 correspond to the midplane, mold corner, and the initial contact of the outer surface with the upper mold wall, respectively ($z/\alpha = 0$, $z/\alpha = 2$, and $r = 1$ in Figure 5). In general, the inflated parison was somewhat thicker at the midplane and the upper wall, and thinner around the mold corner. It is not surprising to see that the thickness distribution obtained with the constant temperature profile is identical to the results obtained in the isothermal case. The meniscus contacts the entire mold cavity before any effects due to heat transfer have a chance to alter the deformation process. Comparatively, in the case of initial natural cooling the parison is slightly thinner along the vertical and horizontal mold walls, becoming much thicker near the upper mold wall ($s \rightarrow 3$) due to the accelerated solidification that takes place there. By imposing a quadratic temperature profile, the meniscus deforms preferentially in the region of hotter material. In this case, the thickness is substantially reduced along the vertical mold wall ($0 \le s \le 2$) and increased along the upper mold boundary ($2 \le s \le 3$).

Comparison with experiments

It is important to validate the computer simulation by comparison to available experiments. By instrumenting the

Table 5. Effect of Initial Temperature Level on Inflation Times and Part Thickness at Midplane, $T_u = 0$

T_M	t_R	t_C	δ_W
1.0	0.4746	7.711	0.0666
1.2	0.3905	6.472	0.0657
1.4	0.3280	5.419	0.0651

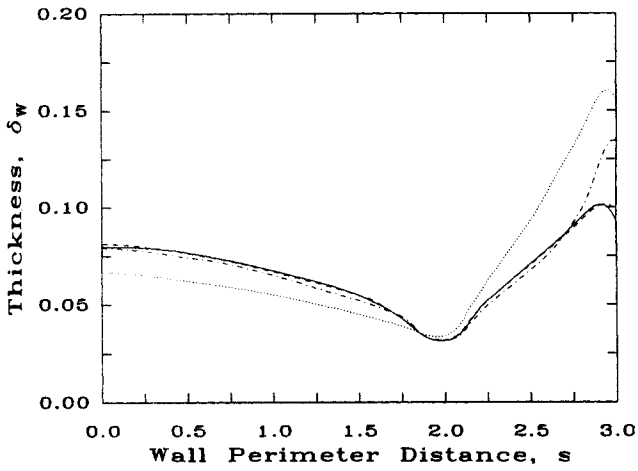

Figure 12. Final thickness distribution of inflated meniscus for a 90° mold corner obtained with various initial temperature distributions.

Case A
___ Isothermal analysis
--- Constant initial temperature, $T = 1$
.... Quadratic initial temperature distribution, $T = 1$, $T_u = 0$
-.-. Initial temperature distribution after natural cooling

injection blow molding apparatus, Haessly (1989) found that the internal pressure was not increased instantaneously; rather, it increased almost linearly over a short time interval before reaching its final present value. This effect was taken into account in the preset analysis by increasing the applied pressure in the following manner:

$$\Delta P(t) = \begin{cases} \Delta P_o(t/t_o) & 0 \le t \le t_o \\ \Delta P_o & t > t_o \end{cases} \qquad (19)$$

where t_o is the dimensionless time at which the applied pressure achieves its final constant value ΔP_o. It was observed that a final pressure of $\Delta P_o = 3 \times 10^5$ (110 psi) was achieved by a dimensionless time of $t_o = 70$ (0.22 s). Using these experimental parameters as input, case B, computer simulations were first carried out for free inflation. It should be noted here that calculations with even larger applied pressures, resulting in larger *Pe* numbers, were also performed without any numerical difficulty. This is because, in spite of the increased *Pe*, convection in the heat balance equation remains small during the very fast inflation due to inappreciable temperature gradients in the parison.

Three different initial temperature profiles were employed:

1. uniform temperature with $T = 1.25$
2. quadratic variation of temperature with $T_M = 1.25$, $T_u = 0$
3. quadratic variation of temperature with $T_M = 1$, $T_u = 0$.

There is significant uncertainty in the experimental measurements of temperatures. Be that as it may, profile 2 seemed to be closer to the experimental measurements than the others.

Figure 13 compares the time evolution of the outer surface at the midplane of the meniscus as predicted by the nonisothermal model to experimental measurements. Although viscoelastic effects have not been included, good agreement is obtained up to the time that the parison radius is almost tripled. At later times a faster inflation rate is predicted and temperature profile 3 exhibits better agreement with experiment. Free inflation for these values of imposed pressure is unstable (Tsamopoulos et al., 1988) and leads to exponential growth of the radius of the meniscus and to its eventual rupture. Therefore, meniscus dynamics become extremely sensitive to the initial conditions. Furthermore, the rapid extension of the meniscus at the latter stages is not correctly captured by the present fluid mechanical model since it does not include the additional resistance due to material elasticity. It is interesting to compare the predicted profiles of the outer free surface to experimental observations, as shown in Figure 14. Although the shapes are obtained at different points in time, the experimental data very closely resemble results obtained with the quadratic temperature distributions 2 or 3. For clarity, only results for case 3 are shown in the figure. The meniscus is observed to bulge near the midplane due to increased temperature imposed in that region. The error bars in the figures represent experimental error.

Figure 15 illustrates the final stages of confined inflation into a 130° mold corner obtained with the present model and the appropriate representation of the mold surface. Based on the previous free inflation analysis, the initial quadratic temperature representation ($T_M = 1.25$, $T_u = 0$) is used in the simulation. It is interesting to note that the meniscus forms two air enclosures with the mold surface; specifically, near the mold corner and along the angled upper mold surface. Well-designated mold configurations must be properly vented, as entrapped air in the mold prevents good contact between the meniscus and the mold wall, resulting in inefficient cooling and poor surface quality of the inflated part. Although air resistance in either surface is neglected, the numerical results may be used to reveal critical aspects of the deformation history and aid in complicated mold design. In the present situation, the meniscus fills the corner first and subsequently contacts the angled wall.

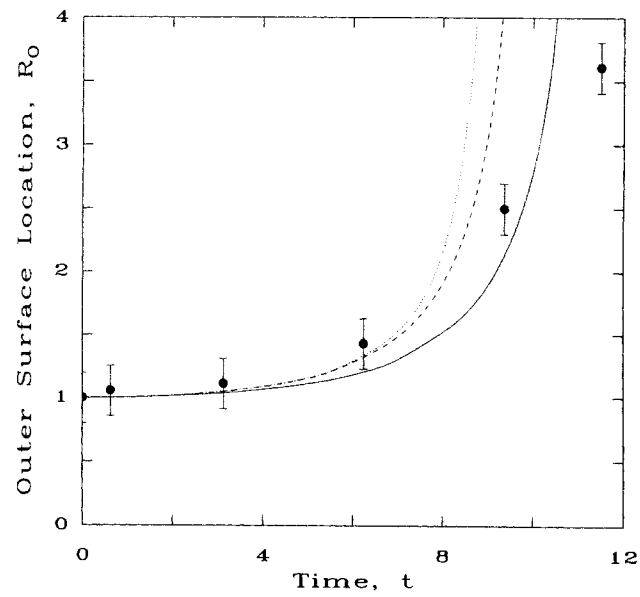

Figure 13. Comparison of theoretical time evolution of outer surface at midplane of meniscus with experiment.

Case B, $T_u = 0$
● Experimental measurements
... Constant initial temperature, $T_M = 1.25$
--- Quadratic initial distribution, $T_M = 1.25$
___ Quadratic initial distribution, $T = 1$

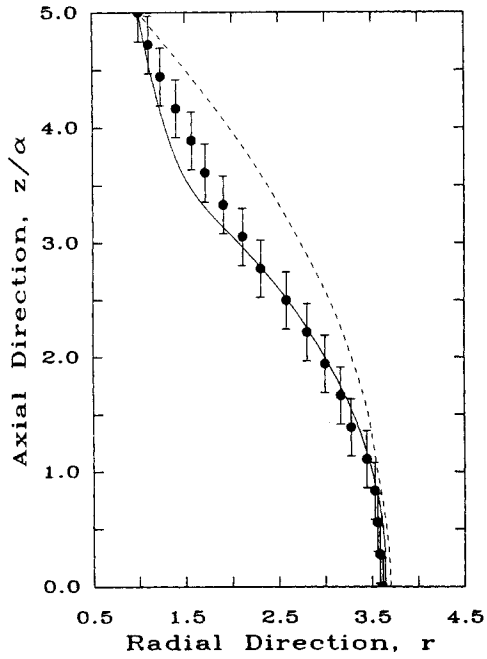

Figure 14. Comparison of instantaneous outer surface profile with experiment.

Case B, $T_u = 0$
● At $t = 11.43$ (experimental)
— At $t = 10.53$ (quadratic initial profile with $T_M = 1.0$)
--- At $t = 8.65$ (constant initial profile with $T = 1.25$)

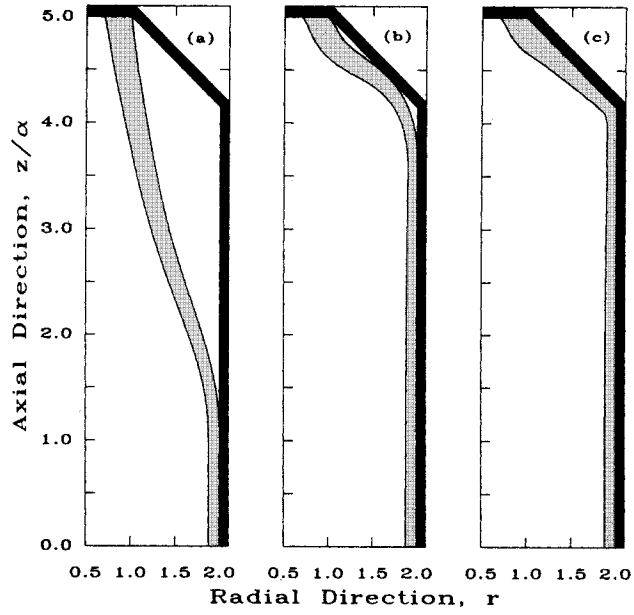

Figure 15. Instantaneous shapes of annular meniscus during confined inflation into a 130° mold corner starting with an initial quadratic temperature distribution

Case B, $T_M = 1.25$, $T_u = 0$
a. $t = 8.57$
b. $t = 11.92$
c. $t = 17.44$

The inflation cycle is completed in 0.0548 s ($t = 17.44$), which is somewhat slower than the experimental value of 0.040 s (Haessly, 1989). In these experiments, however, inflation time and position of the parison in contact with the mold were determined by installing a series of LVDT sensors along the vertical confining wall. Due to equipment configuration, it was not possible to locate a sensor directly in the mold corner; consequently, the experimental inflation time corresponds to an instant slightly prior to complete filling of the mold cavity and thus underpredicts the total inflation time. As before, the limiting step in the production cycle is cooling the meniscus to ambient conditions. Computer simulations reveal that approximately 40 s are required in the present case to reduce the temperature level to the surrounding gas temperature, two orders of magnitude higher than the inflation time.

Figure 16 compares the predicted final thickness distribution to the experimental results. Also shown for comparison is the thickness distribution obtained using isothermal inflation conditions (Poslinski et al., 1991). The theoretical distribution shows good agreement with experiment. The inflated part is observed to be much thicker along the upper angled mold wall ($4 \leq s \leq 5$) than near the midplane ($s = 0$). As expected, the thinnest region is calculated near the mold corner in agreement with experiment. The nonisothermal results show improvement over the isothermal model by predicting a thinner part near the midplane and thicker sections near the upper contact surface. It should also be noted that the experimental data are for a parison of slightly smaller volume. Finally, experiments indicated that asymmetric temperature profiles caused an uneven distribution of the material, suggesting that three-dimensional analysis may need to be performed. Three-dimensional simulations are also necessary if effects of pleating and curtaining are to be considered in accordance with certain experimental observations in extrusion blow molding (Schaul et al., 1975).

Conclusions

Nonisothermal inflation of a viscous annular parison and its subsequent cooling upon wall contact have been simulated with the use of the finite-element method. The algorithm can readily

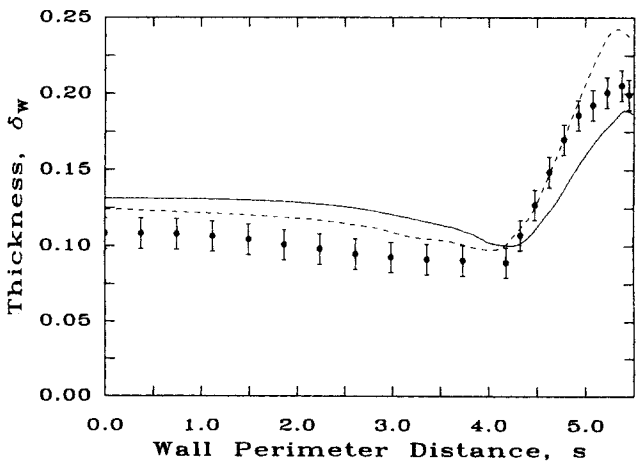

Figure 16. Comparison of final thickness distribution with available experiment for a 130° mold corner.

Case B
● Experimental measurements
— Isothermal initial distribution
--- Quadratic initial distribution, $T_M = 1.25$, $T_u = 0$

be extended to model inflation and cooling for even more complicated configurations in blow molding, as well as other related polymer processing operations. In addition, it may be used to predict inflation times and thickness distribution of the final product as a function of material properties, process conditions and mold configurations. Transient calculations show very good agreement with available experiments, especially for the most important product characteristic, its thickness. Results indicate that the shape of the meniscus during inflation and the quality of the inflated part may be critically affected by the initial temperature distribution in the molten material. The cooling pattern in the meniscus during solidification has a direct bearing on the microstructure of the finished product. Since cooling and solidification take place mainly after contact with the mold, the transients related to momentum transfer may be treated separately from heat transfer transients. This is a quite important simplification if one is to examine viscoelastic effects during the process. One additional advantage of these detailed simulations is that if the blow-molded part is to undergo large stresses during its application as an end product, the predicted wall thickness distribution and its stress and thermal history during production can be used as input in analyzing its strength and expected performance.

Acknowledgment

This research was partially supported by the Fluid Mechanics Program of the National Science Foundation under Grant No. MSM-8705735. Use of the Cornell National Supercomputer facilities (CNSF) is gratefully acknowledged. A. J. Poslinski was also supported by the Graduate Fellowship Program of the Plastics Institute of America, Inc., for part of the research program. D. Orlicki participated in the preliminary stages of software development.

Notation

C_p^o = specific heat at reference temperature $\tilde{T}_o$
e_k = unit base vectors in spherical geometry
$\mathcal{H}_j$ = mean curvature for surface j, $(\tilde{\mathcal{H}}_j\tilde{r}_o)$
k = thermal conductivity
$\tilde{L}$ = length of fluid meniscus
n = unit vector normal to a surface
P_j = gaseous pressure at surface j, $(\tilde{P}_j/\Delta\tilde{P})$
r = radial distance $(\tilde{r}/\tilde{r}_o)$
R_j = interface locations $(\tilde{R}_j/\tilde{r}_o)$
$\tilde{r}_o$ = outer radius of initial cylindrical annulus
R_W = dimensionless radius of vertical mold wall $(\tilde{R}_W/\tilde{r}_o)$
s = mold wall perimeter distance $(\tilde{s}/\tilde{r}_o)$
S = surface area of domain
t = dimensionless time $(\Delta\tilde{P}\tilde{t}/\mu_o)$
T = dimensionless temperature $[(\tilde{T} - \tilde{T}_W)/(\tilde{T}_o - \tilde{T}_W)]$
U = convective heat transfer coefficient
v = dimensionless velocity $[(\mu_o v)/(\tilde{r}_o\Delta\tilde{P})]$
V = total volume of meniscus $(\tilde{V}/\pi\tilde{r}_o^2\tilde{L})$
z = axial distance $(\tilde{z}/\tilde{L})$

Greek letters

$\tilde{\delta}_o$ = initial thickness of cylindrical annulus
δ_W = inflated part thickness $(\tilde{\delta}_W/\tilde{r}_o)$
γ = surface tension of a fluid surface
μ_o = liquid viscosity at reference temperature $\tilde{T}_o$
ρ = density of fluid
σ = dimensionless stress $(\tilde{\sigma}/\Delta\tilde{P})$

Subscripts and superscripts

f = forced convection parameter
G = ambient gas property
I = inner surface variable
M = maximum value
n = natural convection parameter
o = outer surface variable
u = upper wall contact-surface property
W = wall property
$\tilde{}$ = dimensional quantity

Literature Cited

Alexandrou, A. N., N. R. Anturkar, and T. C. Papanastasiou, "An Inverse Finite-Element Method with an Application to Extrusion with Solidification," *Int. J. Num. Meth. Fluids*, **9**, 541 (1989).

Behrens, R. A., M. J. Crochet, C. D. Denson, and A. B. Metzner, "Transient Free-surface Flows: Motion of a Fluid Advancing in a Tube," *AIChE J.*, **33**, 1178 (1987).

———, "Transient Free-Surface Flows: Fluid Advancing through a Bed of Cylinders," *AIChE J.*, **34**, 1894 (1988).

Bird, R. B., R. C. Armstrong, and O. Hassager, *Dynamics of Polymeric Liquids*, 2d ed., **1**, Wiley, New York (1987).

Cesar de Sa, J. M. A., "Numerical Modeling of Glass Forming Processes," *Eng. Comput.*, **3**, 266 (1986).

Cormeau, A., I. Cormeau, and J. Roose, "Numerical Simulation of Glass Blowing," *Numerical Analysis of Forming Processes*, J. F. T. Pittman, O. C. Zienkiewicz, R. D. Wood, and J. M. Alexander, eds., Wiley, New York, (1984).

Christodoulou, K. N., and L. E. Scriven, "Discretization of Viscous Free-Surface Flows and Other Free-boundary Problems," *J. Comput. Phys.*, (Submitted, 1989).

Dantzig, J. A., "Modeling Liquid–Solid Phase Changes with Melt Convection," *Int. J. Num. Meth. Eng.*, **28**, 1769 (1989).

DeLorenzi, H. G., and H. F. Nied, "Blow-molding and Thermoforming of Plastics: Finite-Element Modeling," *Comp. Struct.*, **26**, 197 (1987).

Denson, C. D., "Implications of Extensional Flows in Polymer Fabrication Processes," *Polym. Eng. Sci.*, **13**, 125 (1973).

Derby, J. J., and R. A. Brown, "A Fully Implicit Method for Simulation of the One-Dimensional Solidification of a Binary Alloy," *Chem. Eng. Sci.*, **41**, 37 (1986).

Dussan, V. E. B., "On the Spreading of Liquids on Solid Surfaces: Static and Dynamic Contact Lines," *Ann. Rev. Fluid Mech.*, **11**, 371 (1979).

Edwards, M. F., P. K. Suvanophen, and W. L. Wilkinson, "Heat Transfer in Blow Molding Operations," *Polym. Eng. Sci.*, **19**, 910 (1979).

Ettouney, H. M., and R. A. Brown, "Finite-Element Methods for Steady Solidification Problems," *J. Comp. Phys.*, **49**, 118 (1983).

Fukase, H., A. Iwaaki, and T. Kunio, "A Method of Calculating the Wall Thickness Distribution in Blow-Molded Articles," *SPE Tech. Papers*, **24**, 650 (1978).

Gresho, P. M., R. L. Lee, and R. L. Sani, "On the Time-dependent Solution of the Incompressible Navier-Stokes Equations in Two and Three Dimensions," *Rec. Adv. Num. Meth. Fluids*, **1**, C. Taylor and K. Morgan, eds., Pineridge, Swansea, U.K., 27 (1983).

Gutfinger, C., E. Broyer, and Z. Tadmor, "Melt Solidification in Polymer Processing," *Polym. Eng. Sci.*, **15**, 515 (1975).

Haessly, W. P., "Finite-Element Modeling and Experimental Study of Injection Blow Molding," Ph.D. Thesis, Dept. Chem. Eng., Univ. Buffalo, New York (1989).

Kamal, M. R., and D. Kaylon, "Heat Transfer and Microstructure in Extrusion Blow Molding," *Polym. Eng. Sci.*, **23**, 503 (1983).

Kamal, M. R., V. Tan, and D. Kaylon, "Measurement and Calculation of Parison Dimensions and Bottle Thickness Distribution During Blow Molding," *Polym. Eng. Sci.*, **21**, 331 (1981).

Kamal, M. R., S. K. Goyal, and E. Chu, "Simulation of Injection Mold Filling of Viscoelastic Polymer with Fountain Flow," *AIChE J.*, **34**(1), 94 (1988).

Keunings, R., "An Algorithm for the Simulation of Transient Viscoelastic Flows with Free Surfaces," *J. Comp. Phys.*, **62**, 199 (1986).

Kheshgi, H. S., and L. E. Scriven, "Penalty Finite-element Analysis of Unsteady Free-surface Flows," *Finite Elements in Fluids*, **5**, R. H. Gallagher, J. T. Oden, O. Zienkiewicz, T. Kawai, and M. Kawahara, eds., Wiley, New York (1984).

Kistler, S. F., and L. E. Scriven, "Coating Flow," *Computational Analysis of Polymer Processing*, J. R. A. Pearson and S. M. Richardson, eds., Appl. Science Pub., New York, 243 (1983).

Petrie, C. J. S., "Film Blowing, Blow Molding, and Thermoforming," *Computational Analysis of Polymer Processing*, J. R. A. Pearson and S. M. Richardson, eds., Appl. Science Pub., New York, 217 (1983).
Poslinski, A. J., "A Finite-Element Analysis of the Inflation and Cooling Stages in Blow Molding Operations," Ph.D. Thesis, Dept. Chem. Eng., State Univ. New York, Buffalo (1990).
Poslinski, A. J., and J. A. Tsamopoulos, "Inflating Dynamics of Fluid Annular Menisci Inside a Mold Cavity. I: Deformation Driven by Small Gas Pressures," *Chem. Eng. Sci.* **46,** 215 (1991).
Poslinski, A. J., D. Orlicki, and J. A. Tsamopoulos, "Inflation Dynamics of Fluid Annular Menisci. II: Deformation Driven by Large Gas Pressures," *Chem. Eng. Sci.* **46,** 597 (1991).
Ryan, M. E., and A. Dutta, "Mathematical Modeling of the Blow-Molding Process," *Polym. Eng. Sci.*, **22,** 1075 (1982).
Schaul, J. S., M. J. Hannon, and K. F. Wissbrun, "Analysis of Factors Determining Parison Properties in High Shear Rate Blow Molding," *Trans. Soc. Rheol.*, **19**(3), 351 (1975).
Schlichting, H., *Boundary-Layer Theory*, 7th ed., McGraw-Hill, New York (1979).
Strang, G., and G. Fix, *An Analysis of the Finite-Element Method*, Prentice Hall, Englewood Cliffs, NJ (1973).
Tadmor, Z., and C. G. Gogos, *Principles of Polymer Processing*, Wiley, New York (1979).
Talmon, Y., H. T. Davis, and L. E. Scriven, "Progressive Freezing of Composites Analyzed by Isotherm Migration Methods," *AIChE J.*, **27**(6), 928 (1981).
Tanner, R. I., *Engineering Rheology*, Oxford, p. 4 New York (1985).
Thomas, P. D., and R. A. Brown, "LU-decomposition of Matrices with Augmented Dense Constraints," *Int. J. Num. Meth. Eng.*, **24,** 1451 (1987).
Tsamopoulos, J. A., T. R. Akylas, and R. A. Brown, 'Dynamics of Charged Drop Break-Up," *Proc. R. Soc. Lond.*, **A401,** 67 (1985).
Tsamopoulos, J. A., A. J. Poslinski, and M. E. Ryan, "Equilibrium Shapes and Stability of Captive Annular Menisci," *J. Fluid Mech.*, **197,** 523 (1988).
Ungar, L. H., N. Ramprasad, and R. A. Brown, "Finite-Element Methods for Unsteady Solidification Problems Arising in Prediction of Morphological Structure," *J. Sci. Comp.*, **3,** 77 (1988).
Wu, S., "Interfacial and Surface Tensions of Polymers," *J. Macromol. Sci.—Revs. Macromol. Chem.*, **C10,** 1 (1974).

Manuscript received May 22, 1990, and revision received Oct. 1, 1990.